Supporting Information

Hoyer et al. 10.1073/pnas.1522292113

SI Materials and Methods

Optical Setup. Our LS-RESOLFT nanoscope uses laser beams of three fast-switching continuous-wave diode lasers which are formed to LSs in the focal plane of the water-dipping illumination objective (CFI Plan Fluor 10XW, Nikon, N.A. 0.3). Light of a UV laser (iBeam Smart 405–60, Toptica Photonics) with a nominal wavelength of 405 nm and maximal power of 60 mW activates RSFPs in the sample. The off-switching light pattern is generated by a second diode laser (iBeam Smart PT488-50, Toptica Photonics, 488 nm, 50 mW). After the off-switching process, the remaining activated RSFPs are read out using a third laser (LuxX 488–60, Omicron-Laserage Laserprodukte, 488 nm, 60 mW) with the same nominal wavelength. The lasers are spectrally and spatially filtered with narrow bandpass filters (FF02-482/18–25, FF01-406/15–25, Semrock) and polarization-maintaining single-mode fibers (M460-HP, Thorlabs), respectively. At the fiber output, the beam diameter of each laser is independently controlled with achromatic doublets to compensate for potential longitudinal chromatic aberrations in the focal plane. The off-switching intensity pattern is generated by a half-moon phase plate which is placed on the optical axis of the collimated off-switching laser beam (Fig. S1 *E* and *F*). It consists of two quartz blocks mounted in parallel on a multiaxis positioner (LP-1A, Newport Corporation), which tilts the blocks with respect to each other to generate a phase difference between the beam halves. The modified beam is subsequently combined with the beam path of the readout laser by a 50:50 beam-splitting cube (BS013, Thorlabs). A dichroic mirror (Di02-R442, Semrock) merges the expanded UV beam with the readout and the off-switching laser. A common beam expander consisting of two achromatic lenses adjusts the beam widths to the pupil diameter of the illumination objective. The polarization state of the laser beams for activation, excitation, and switch-off is adjusted by a Glan–Thompson prism (PGT 1.10, B. Halle) and a half-wave plate, and the zero-intensity region's characteristics evaluated on gold particles (Fig. S3 *G*–*J*). A cylindrical lens (f_{CL} = 150 mm) focuses the collinear beams into the back-aperture of the illumination objective, which generates an LS at an angle $\beta = 30°$ with respect to the horizontal plane. The detection objective (CFI Apo 40XW NIR, Nikon, N.A. 0.8) is oriented perpendicular to the *x*-*y* plane of the LS and thus has an angle of 60° with respect to the coverslip. These angles were chosen such that, theoretically, any commercially available water-dipping detection objective lens today can use its full aperture for collection of fluorescence light. Additionally, undesired artifacts potentially caused by direct reflections of the illumination laser light from the coverslip surface are reduced. Both the illumination and detection objectives are held by a monolithic objective mount unit which is connected to a standard breadboard by a kinematic mount consisting of a system of balls, vee-grooves, and magnets, and can be lifted for conveniently replacing the sample or the objectives (Fig. S1*B*). The objective lenses can be moved along their optical axes by linear stages (M-SDS40 Precision, Newport Corporation). The relative lateral position of the objectives can be precisely adjusted with a home-built flexure design. The detection objective is part of a wide-field microscope consisting of two identical emission bandpass filters (FF03-525/50–25, Semrock) and a tube lens (f_{TL} = 300 mm, Nikon) focusing the fluorescence onto a 4-megapixel (2,048 × 2,048 pixels) sCMOS camera (ORCA-Flash4.0 V2, Hamamatsu). The focal length of the tube lens was chosen such that the 6.5-μm square pixels on the camera projected to a sampling size of 108.3 nm in the specimen space. For optimal LS-RESOLFT imaging speed, the camera is rotated by β so that the readout lines of the sensor are aligned along the *x* direction. A cropped FOV along the *y* direction thus considerably shortens the required readout time and increases the overall frame rate. For imaging, a standard round glass coverslip with a diameter of 5 mm is clipped onto a platform at the bottom of a medium-filled specimen chamber made of biocompatible polyetheretherketone (PEEK), which features a comparably low linear thermal expansion coefficient and excellent resistance to a wide range of chemicals (Fig. S1 *C* and *D*). On one side of the chamber, a glass window is inserted, through which the LSs can be imaged from the side (Fig. 1 *B*, *D*, and *F*). To accurately and reproducibly align the longer horizontal axis of the specimen chamber relative to the scan direction, its lateral movement is kinematically constrained by a system of balls, vee-grooves, and magnets. A piezoelectric stage (P-625.1CL, PIHera Piezo Linear Stage, Physik Instrumente) with a minimal step size of 10 nm and a total range of 500 μm scans the sample in steps through the static LSs. A preset step response time of 102 ms/μm assures a stable scan throughout the measurement. The scanner is attached to a multiaxis positioning stage (562 ULTRAlign Precision, Newport Corporation), with which the sample can be centered in the FOV of detection.

Image Acquisition and Representation. All electronic devices in the setup, i.e., lasers, camera, and the stage scanner are controlled by custom software composed in LabVIEW. An FPGA (field-programmable gate array) (NI PCIe-7841R, National Instruments) simultaneously sends a predefined sequence of analog and digital signals to the devices to assure synchronization of the scanning process and image acquisition. For a single 2D LS-RESOLFT image, a sequence of three successive laser triggers is used: First, molecules are switched to the on state ("activation") with an LS at 405 nm. Then, a short illumination pause of 2 ms is followed by an off-switching pulse, which is typically longer than the activation period. After another pause of 2 ms, signal for the actual subdiffraction LS-RESOLFT image is acquired while illuminating the sample with the excitation laser at 488 nm, and stored on a separate camera PC. We set the total acquisition time per scanning step to 94 ms (activation, 10 ms; off-switching, 30 ms; readout, 50 ms) and 174 ms (10 ms, 100 ms, 60 ms) for rsEGFP2 and rsEGFP(N205S) samples, respectively. To directly visualize the resolution improvement by LS-RESOLFT, a conventional diffraction-limited LSFM image is taken in a second activation and readout cycle with the same exposure time and light intensity. Finally, the stage scanner moves to the next position where another illumination cycle starts. By translating the scanner only in the horizontal plane, the biological sample always remains positioned at the minimal LS waist. This ensures that the sample is imaged with the same axial resolution at any scan position. In principle, a very large area (i.e., volume), up to the maximal scanning range of the scanner, can be imaged with this method.

Image data recorded in RESOLFT nanoscopes and standard LS typically do not require any postprocessing such as fitting, denoising, or restoration. The excellent signal-to-noise ratio characteristic for both techniques corroborates this fact. Their combination in LS-RESOLFT nanoscopy benefits from these advantages. The strength of the new instrument is best demonstrated in image cross-sections perpendicular to the optical axis of the LSs. Single slices in the *x*-*z* and *y*-*z* planes are of particular interest for ascertaining the achieved axial resolution of the LS-RESOLFT method. In projections of maximum intensity of multiple slices along *y* and *x*, respectively, the separation of objects with a distance below the diffraction limit can

be demonstrated. For this, the recorded images are affinely transformed to the coordinate system of the LS using a custom MATLAB script (Fig. S2). It should be noted that this procedure rearranges the acquired data without changing its raw character.

HIV-1 Particle Preparation. The pCHIV-rsEGFP2 plasmid was derived from pCHIV (31), which contains the complete HIV-1 coding sequence except for *nef* with deletions in noncoding regions rendering it noninfectious. The rsEGFP2 coding sequence was inserted close to the 3′ end of the matrix coding region of the structural *gag* gene as previously described for other fluorescent proteins (32). Using polyethylenimine as transfection reagent, 293 T cells were transfected in a 1:1 ratio with the pCHIV and pCHIV-rsEGFP2. Two days posttransfection the cellular supernatant was harvested and purified by ultracentrifugation through a 20% (wt/vol) sucrose cushion at 130.000 × *g* for 90 min at 4 °C. Particle pellets were resuspended in PBS and stored at −80 °C. A standard round glass coverslip was cleaned with absolute ethanol and air-dried. A drop of HIV-1 particles diluted in PBS was incubated on the coverslip for 10 min. The coverslip was then carefully rinsed with PBS. HIV-1 samples were imaged at room temperature in FluoroBrite DMEM.

Mammalian Cell Culture. A pool of transiently transfected and subsequently FACS-sorted HeLa Kyoto cells expressing keratin-19-rsEGFP(N205S) was grown in DMEM containing phenol red, L-glutamine, and high glucose supplemented with 10% (vol/vol) FBS, 1% sodium pyruvate, and geneticin selective antibiotic at a final concentration of 1 mg/mL. For live-cell experiments with the LS-RESOLFT nanoscope, ∼1×10^5 cells were seeded on a round coverslip in a 24-well and grown for 24 h. Three hours before imaging, the selection medium was exchanged by DMEM containing Hepes (but no phenol red, to reduce unwanted background caused by phenol red uptake). Immediately before imaging, the coverslip was washed with PBS. The cells were imaged at room temperature in FluoroBrite DMEM. U2OS cells were grown in McCoy's 5A modified medium containing phenol red, L-glutamine, high glucose, and bacto-peptone supplemented with 1% FCS, 1% glutamine, 1% nonessential amino acids, and 1% penicillin streptomycin. For live-cell LS-RESOLFT imaging, 4×10^4 cells were grown on a round coverslip placed in a 24-well for 24 h. Then, the cells were transiently transfected with the construct NUP214-3x-rsEGFP(N205S) and FugeneHD according to the manufacturer's guidelines. After an incubation time of 72 h, the growth medium was exchanged by DMEM containing Hepes but no phenol red. Immediately before imaging, the coverslip was washed three times with PBS. The cells were imaged at room temperature in FluoroBrite DMEM. To obtain the NUP214-3x-rsEGFP(N205S) construct, the DNA of the NUP214-gene was amplified per PCR from a pNUP214-EGFP plasmid and subcloned into a backbone that was obtained before by introducing a triple-rsEGFP(N205S) into a pmEGFP-N1 vector.

Calculation of the Gain in Speed by LS-RESOLFT Over Z-Doughnut RESOLFT Strategies. LS-RESOLFT nanoscopy offers highly parallelized 3D imaging with subdiffraction axial resolution. In the technical realization presented here, the LSs are generated such that the FOV in the x direction is solely determined by the physical size of the camera chip in this direction $s_{x,cam}$ and the overall magnification of the detection path M_{det}:

$$\mathrm{FOV}_x = \frac{s_{x,cam}}{M_{det}} = m \cdot \frac{p_{x,cam}}{M_{det}} = m \cdot d_x,$$

where m is the number of acquired pixel columns, $p_{x,cam}$ is the physical size of a camera pixel in x, and d_x is the sampling size of the detection focal plane in x. The FOV in the y direction is defined by twice the Rayleigh range y_R of the LSs in illumination direction:

$$\mathrm{FOV}_y = 2 \cdot y_R = n \cdot \frac{p_{y,cam}}{M_{det}} = n \cdot d_y.$$

Here, n denotes the number of pixels in the y direction, $p_{y,cam}$ is the physical size of a camera pixel in y, and d_y is the sampling size of the detection focal plane in y.

Typically M_{det} is set such that the lateral sampling of the acquired image is at least threefold higher than the diffraction limit to fulfill the Nyquist sampling criterion. For squared pixels $p_{x,cam} = p_{y,cam} = p_{cam}$, and $d_x = d_y = d$.

The LS-RESOLFT nanoscope presented here acquires a single plane in one switching cycle with a switching time t, a pixel size of 6.5 μm, a magnification $M_{det} = 60$, and a lateral sampling in x and y of $d_{LS} = 108.3$ nm.

For a fair comparison we assume a point-scanning RESOLFT nanoscope which achieves the same subdiffraction axial resolution using a z-doughnut off-switching light pattern generated through a high-N.A. objective. The lateral resolution may be limited to 240 nm by diffraction, which results in a lateral sampling size of $d_{PS} = 240\ \mathrm{nm}/3 = 80$ nm. For the same switching kinetics of the fluorophores the pixel dwell time is t.

The gain G in speed by LS-RESOLFT nanoscopy compared with a z-doughnut RESOLFT strategy for the same FOV and subdiffraction axial resolution is then

$$G = \frac{T_{PS}}{T_{LS}} = \frac{m \cdot n \cdot d_{PS}^2 \cdot t}{d_{LS}^2 \cdot t} = \frac{m \cdot n \cdot d_{PS}^2}{d_{LS}^2},$$

where T_{PS} and T_{LS} are the respective total acquisition times for one plane. For a maximal FOV of 221 × 28 μm^2, we obtain a gain factor of 279,378.

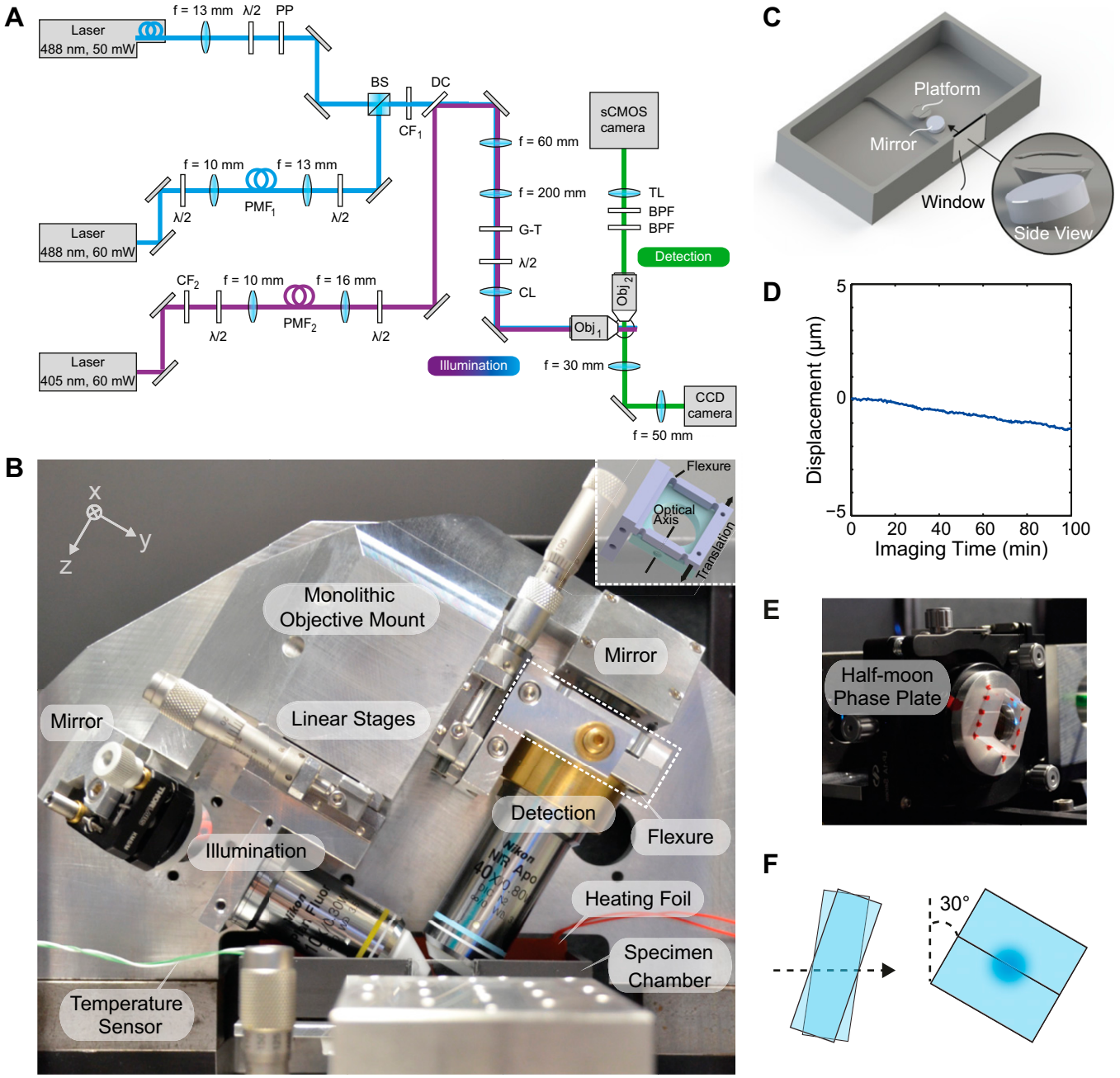

Fig. S1. LS-RESOLFT setup. (*A*) Diagram of the optical components and the beam paths. λ/2: Half-wave plate polarization retarder, B. Halle Nachfl., PP: Half-moon phase plate, B. Halle Nachfl., Germany; BS: 50:50 beam-splitter cube, Thorlabs; PMF_1: Polarization-maintaining single-mode fiber, Thorlabs; CF_1: Excitation clean-up filter, 482/18, Semrock; CF_2: Excitation clean-up filter, 406/15, Semrock; PMF_2: Polarization-maintaining single-mode fiber, Thorlabs; DC: Dichroic mirror, Di02-R442, Semrock; G-T: Glan–Thompson prism, B. Halle Nachfl.; CL: Cylindrical lens, f = 150 mm, Thorlabs; Obj_1: Objective lens CFI Plan Fluor 10XW, N.A. 0.3, Nikon; Obj_2: Objective lens CFI Apo 40XW NIR, N.A. 0.8, Nikon; BPF: Fluorescence bandpass filter, 525/50, Semrock; TL: Tube lens, f = 300 mm, Nikon. (*B*) Monolithic objective mount unit for LS-RESOLFT. The illumination objective lens creates an LS which illuminates the sample in the specimen chamber at an angle of 30°. Fluorescence is collected by a detection objective lens perpendicular to the illumination axis. Both lenses are mounted on the same aluminum block to reduce thermal drifts. They are translated along their respective optical axes by linear stages (in *y* and *z*). For lateral positioning of the objective lenses (in *x*) a flexure is used (highlighted by a white dashed frame). (*Inset*) CAD drawing and the translation axis of the flexure. The imaging medium can be heated with a silicon-coated foil which is placed in the specimen chamber. The temperature is controlled by a sensor in the medium. (*C*) Specimen chamber. A standard round coverslip (diameter of 5 mm) with the sample is placed on a platform in the center of the cuboid-shaped specimen chamber made of PEEK. An imaging medium containing essential nonfluorescent additives for cell growth and Hepes buffer, and a temperature control adapt the conditions in the chamber to the physiological environment of living specimens. (*D*) The LS reflection on a tiny mirror placed at 15° with respect to the horizontal plane is used to measure the stability of the chamber. A displacement of less than 0.7 µm in 60 min is extracted from the plot. (*E*) Mounting and positioning of the half-moon phase plate. The half-moon phase plate consists of two glass flats mounted side-by-side, with one flat being tilted about an axis perpendicular to the touching faces. This assembly as a whole can be tilted about the same axis. (*F*) The off-switching beam is aligned to the optic axis, which is defined by the interface of the touching faces and the axis of tilt. For a fixed relative angle of the flats, a particular common tilt angle can be found such that the phase of one-half of the incident beam is retarded by π relative to the other half. The phase plate is rotated by 30° to account for the angle of the illumination objective.

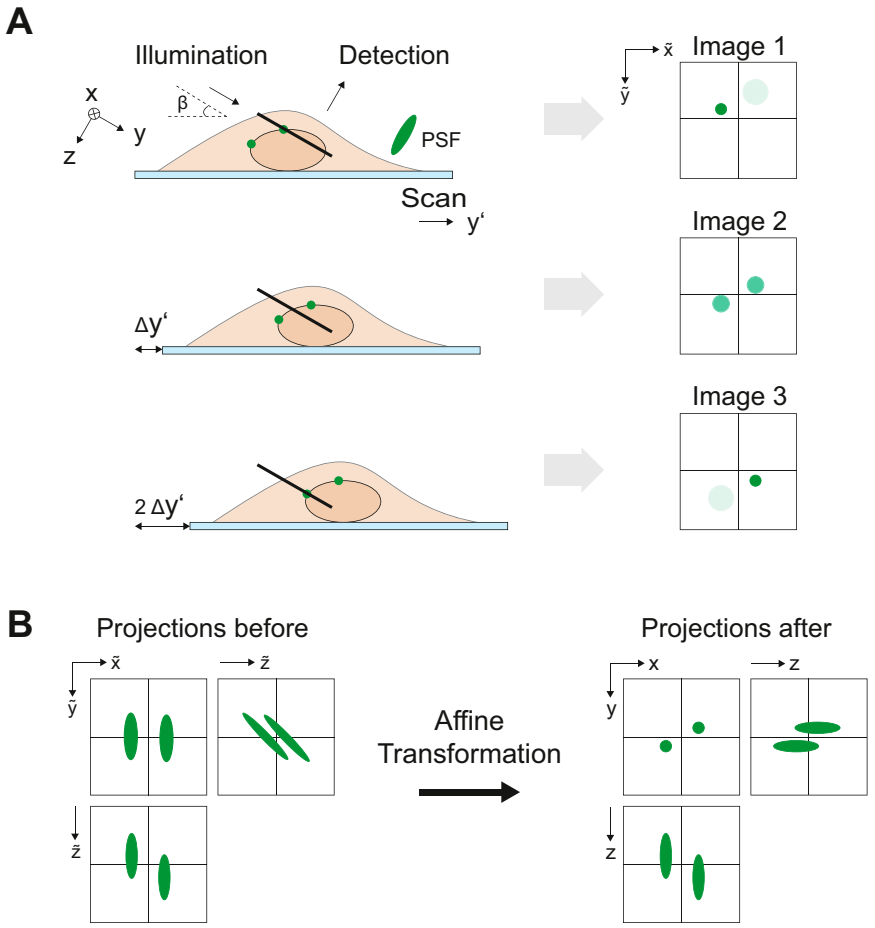

Fig. S2. Representation of LS-RESOLFT images. (*A*) A sample with two fluorophores is scanned in the y′ direction through the static illumination LS, which makes an angle β with the horizontal plane. For clarity, the point-spread function (PSF) after off-switching is here depicted elongated along the *z* axis. Three steps of the scanning process are illustrated. The resulting images taken in the FOV of the camera (black line) are shown on the right. (*B*) The acquired image stack is affinely transformed to the coordinate system of the objective lenses using

$$\begin{pmatrix} x \\ y \\ z \end{pmatrix} = \begin{pmatrix} 1 & 0 & 0 \\ 0 & 1 & a \\ 0 & 0 & 1 \end{pmatrix} \begin{pmatrix} \tilde{x} \\ \tilde{y} \\ \tilde{z} \end{pmatrix}, \text{ with } a = \frac{\Delta y'}{p_{x,y}} \sin 60°.$$

Thus, the axial and lateral extent of the resultant PSF is directly visible in the resulting maximum intensity projections. Note that the affine transformation does not change the raw character of the LS-RESOLFT images. Note that, for better visualization, images have typically been represented with anisotropic pixels (pixel dimensions stated in figures). Versions with isotropic pixels can be found in Fig. S10.

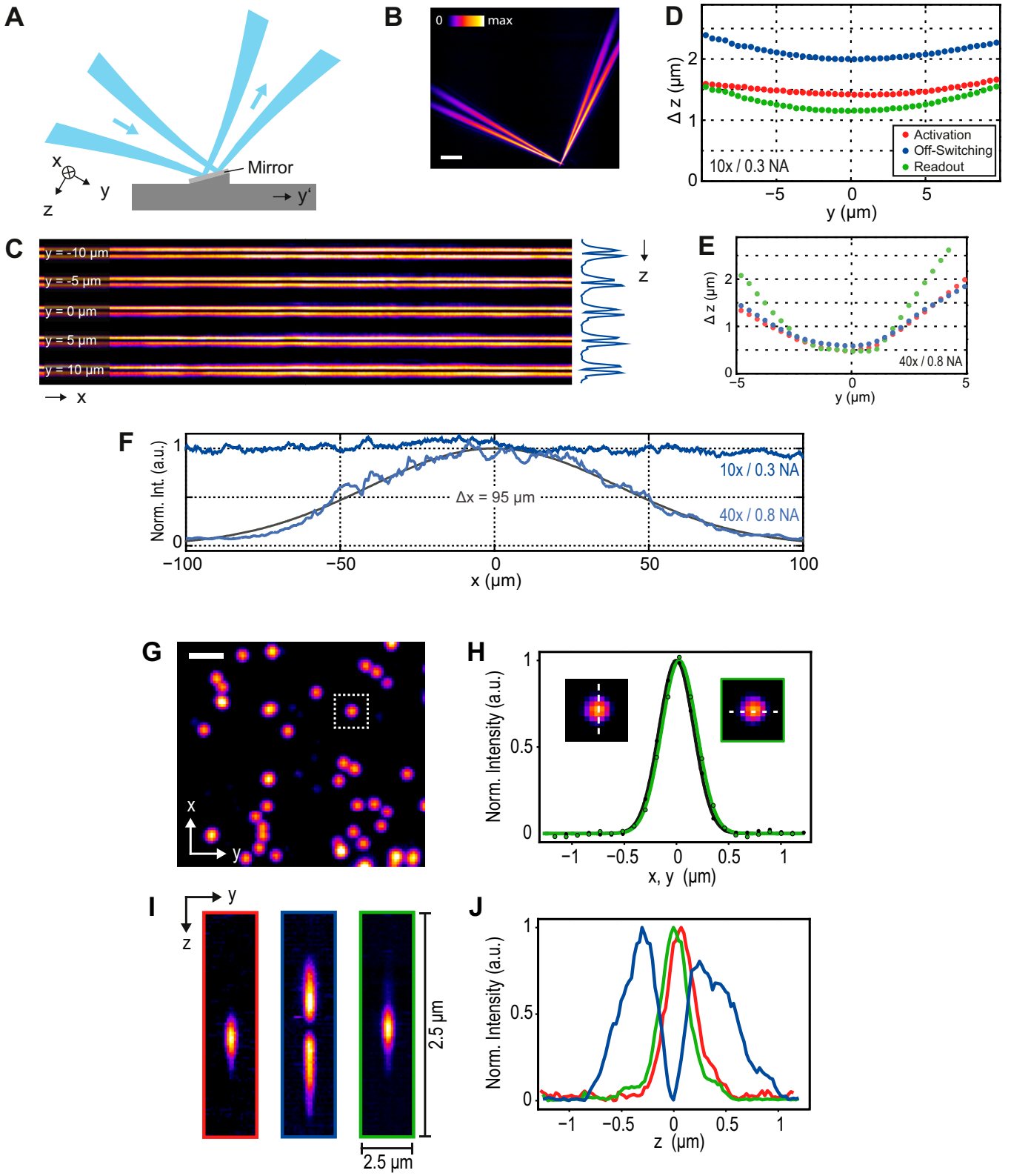

Fig. S3. (*A–F*) Measurement of LS parameters. A mirror in the LS-RESOLFT specimen chamber (Fig. S1 *C* and *D*) reflects the attenuated static off-switching LS generated by a 10×/0.3 N.A. objective lens, as shown in the sketch (*A*) and the measured *y-z* cross-section (*B*). (Scale bar, 100 μm.) To measure the dimensions of the LS, the mirror is scanned stepwise in the *y'* direction. At each scanning position, the reflected light is collected by a 40×/0.8 N.A. objective lens and imaged onto the sCMOS camera, resulting in *x-z* cross-sections of the LS after affine transformation. Five images of positions around the LS focus at $y = 0$ are shown in a montage (*C*). A line profile along the *z* axis across the integrated LS intensity reveals a reasonably uniform LS thickness over the extent of the typical spatial dimension of a biological cell. (*D*) The axial widths of all applied LSs in the presented study are plotted versus the illumination axis *y*. Their Rayleigh lengths were measured to be 6.5× longer than those measured for LSs generated by (*E*) a 40×/0.8 N.A. illumination objective lens, which results in a larger FOV along

Legend continued on following page

the *y* direction. (*F*) The lateral extent along the *x* direction of an off-switching LS is plotted for both illumination objective lenses. A Gaussian fit to the higher-N.A. intensity profile (which was not applied in LS-RESOLFT) reveals an FWHM of 95 μm, whereas the low-N.A. LS used for LS-RESOLFT imaging uniformly covers the entire FOV of the camera. The data for the sheets generated with a 40×/0.8 N.A. illumination lens are displayed for comparison only. (*G*–*J*) Measurement of the system's PSFs and analysis of the zero-intensity region. Gold colloids on a glass coverslip scatter light of the laser LSs generated by a 40×/0.8 N.A. illumination objective, which is then imaged onto an sCMOS camera. (*G*) An overview image in the *x*-*y* plane shows the gold colloids (80 nm; BBI Solutions) imaged with the readout LS. (Scale bar, 1.5 μm.) (*H*) Line profiles in *x*- and *y* direction through a gold colloid image are shown. Gaussian fits to the data points reveal an FWHM in *x* (green dots and curve) and *y* (black) of 390 and 394 nm, respectively. (*I*) A *y*-*z* projection (2.5 × 2.5 μm^2) of a gold colloid imaged with the activation (red), off-switching (blue), and readout (green) LS is shown. Note that the sampling size in *z* is 25 nm, whereas the sampling size in *y* is 108.3 nm (square image dimensions). The off-switching illumination profile clearly features an intensity minimum in the center. (*J*) Line profiles through projections in *I* along *z* show that the minimum is close to the background signal, which allows for LS-RESOLFT images with a potentially high signal-to-noise ratio. Despite a slight displacement from the center, the activation and readout peaks fully cover the off-switching zero-intensity position. Gaussian fits to their profiles exhibit FWHM values of 326 and 318 nm, respectively. Note that a bandpass filter was inserted to block light scattered by the coverslip. To attain reasonable signal-to-noise ratios in the images, we had to use sufficiently high intensities at the gold particles that could—for our available overall laser power—only be created by the higher-N.A. illumination, such as by the 40× (0.8 N.A.) lens, which was used for this demonstration.

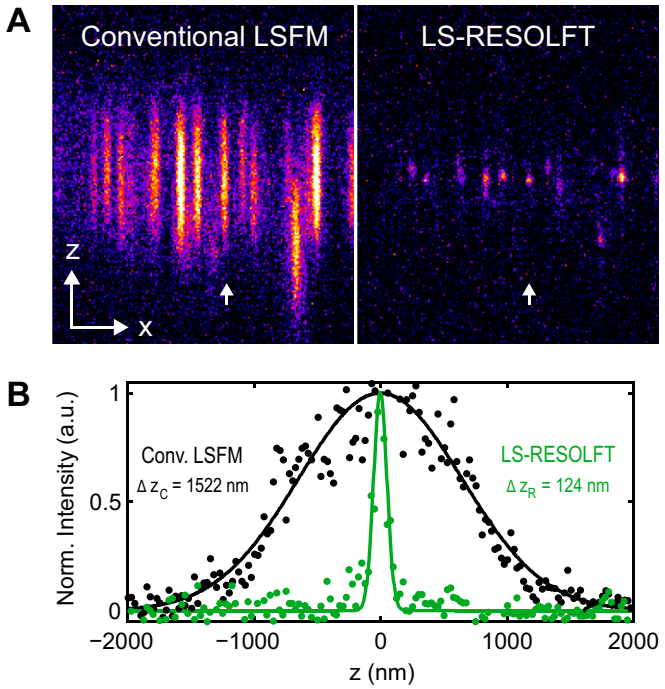

Fig. S4. Resolving power of the LS-RESOLFT nanoscope. (*A*) The resolving power of the LS-RESOLFT nanoscope is measured on single HIV-1 particles on a glass coverslip. An *x*-*z* cross-section through a typical 3D image stack clearly shows the improvement in *z* resolution enabled by the LS-RESOLFT method compared with conventional LSFM. Note that the pixel size in both images is 108.3 nm in *x*- and 25 nm in *z* direction, and overall image dimensions are 19 × 5 μm^2. (*B*) The pixel intensity along a line in the *z* direction through the same single virus particle is plotted for conventional LSFM (black dots) and LS-RESOLFT (green dots), respectively. The *x* position of the line profiles is marked with white arrows in the images. The FWHMs of Gaussian fits to the data reveal an improvement in axial resolution by LS-RESOLFT by a factor of 12.3 compared with standard LSFM.

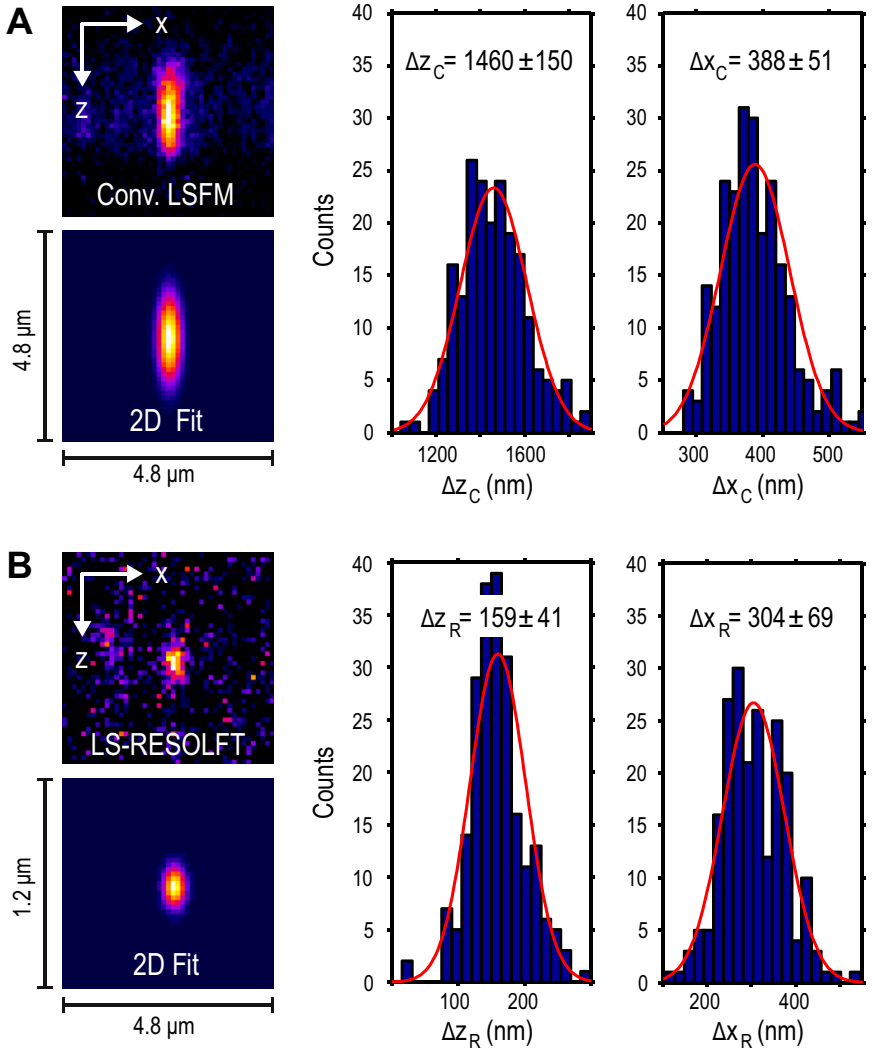

Fig. S5. Distribution of axial and lateral FWHMs of Gaussian fits to HIV-1 particles imaged in conventional LSFM and LS-RESOLFT mode. (*A*) The FWHMs in *z* and *x* were extracted from more than 200 2D fits to conventional LSFM images of single HIV-1 particles on a glass coverslip. A typical image and the corresponding fit are shown on the left. From a fit to the distribution of FWHMs, the peak positions and SDs are determined. (*B*) The same region was scanned at maximal off-switching power in LS-RESOLFT mode. Two hundred and ten fits in *z* and *x*, respectively, were analyzed. Here, the resolving power in the *z* direction averaged over the FOV is improved by a factor of 9.2. Also, the lateral sharpness of particle images in LS-RESOLFT is improved by ∼15–20%. Note that for a valid fit, the 45 × 45 pixels of the images have different scales. In LS-RESOLFT images the pixel size in *z* is 25 nm, whereas the pixel size in *x* and the pixel size in both dimensions in conventional LSFM images is 108.3 nm.

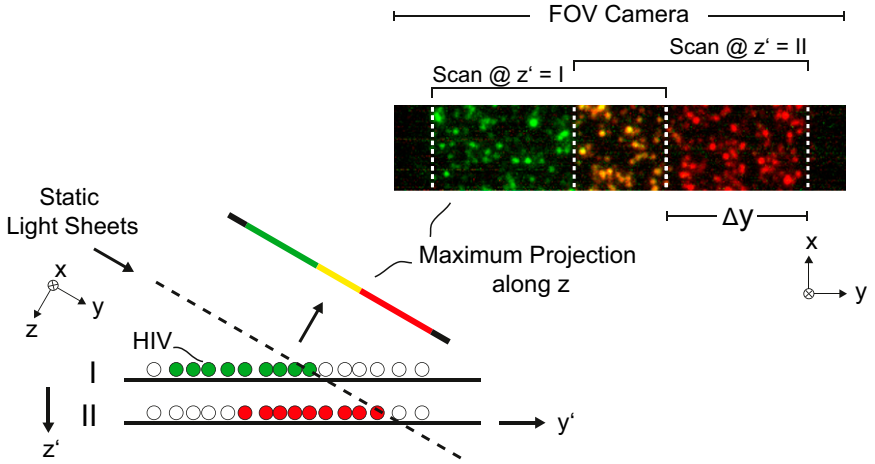

Fig. S6. Method to determine the Rayleigh range of the effective RESOLFT LS. The experiment was intended to measure the Rayleigh range of the effective fluorescence LS which is created by switching off RSFPs above and below the focal plane of detection with LS-RESOLFT. To this end, the average axial FWHM of imaged rsEGFP2-filled HIV-1 particles was determined at several positions along the optical illumination axis (*y*) of the applied LSs. The distance between two *y* positions, denoted as Δ*y*, is not directly given by the setup, but it can be determined from the measured data. This sketch depicts the data analysis for the example of one particular Δ*y*. It is assumed that at a vertical position of the sample $z' = \mathrm{I}$, the LS hits the HIV-1 particles on the coverslip at the position of minimal beam waist along the *y* direction. The sample is scanned and imaged with the same parameters as described in the single-HIV-1 experiment. In the next step of the experiment, the sample is moved downward to $z' = \mathrm{II}$. At the position where the LS hits the sample, the LS thickness is increased. The sample is scanned with the same parameters as in the first step. After an affine transformation as described in Fig. S2, the maximum projections along the *z* axis of both image stacks are color coded and overlapped. White dashed lines in the figure mark the start and the end of the scanned FOV for each scan step. The distance between the start positions of the two scans is equal to the distance Δ*y* of the second scan position to the position of minimal beam waist along the optical illumination axis.

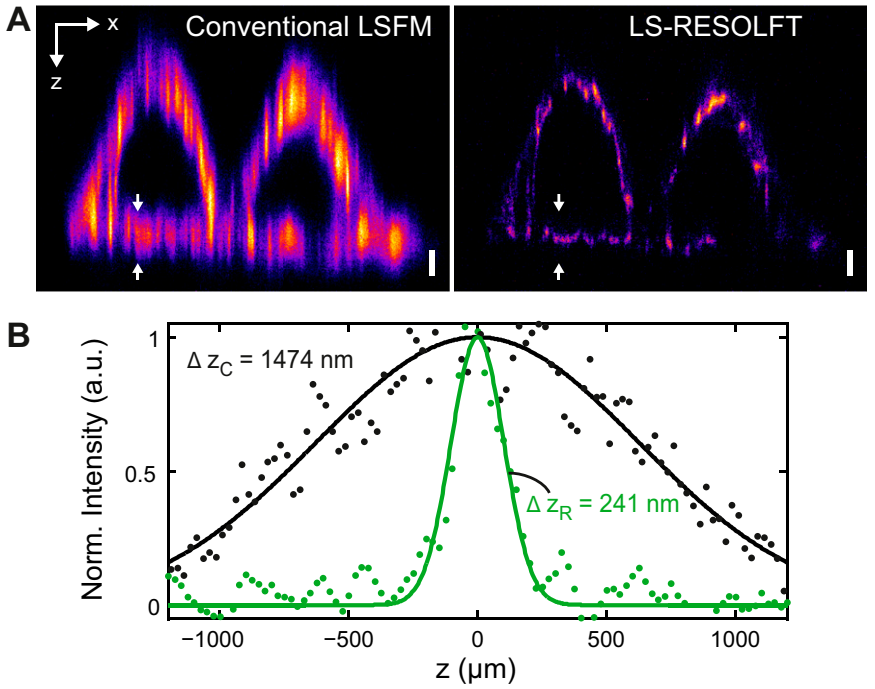

Fig. S7. LS-RESOLFT of the intracellular keratin network in living cells. (*A*) The superior axial resolution of our LS-RESOLFT nanoscope compared with conventional LSFM is demonstrated on a single keratin-19 filament tagged with rsEGFP(N205S) in a HeLa cell. An *x*-*z* cross-section through the same image stack as displayed in Fig. 3 *A*–*C* clearly shows the improved *z* resolution. The image dimensions are $70 \times 11\ \mu m^2$ with a pixel size in both images of 108.3 nm in *x*- and 25 nm in the *z* direction. (Scale bar width and height, 1 μm.) (*B*) The axial intensity profile along a line through the same single keratin-19 strand is plotted for conventional LSFM (black dots) and LS-RESOLFT (green dots), respectively. The *x* position of the line profiles is marked by white arrows in the images. LS-RESOLFT here improves the axial resolution by a factor of 6.1 compared with conventional LSFM, as revealed by the FWHMs of Gaussian fits to the data.

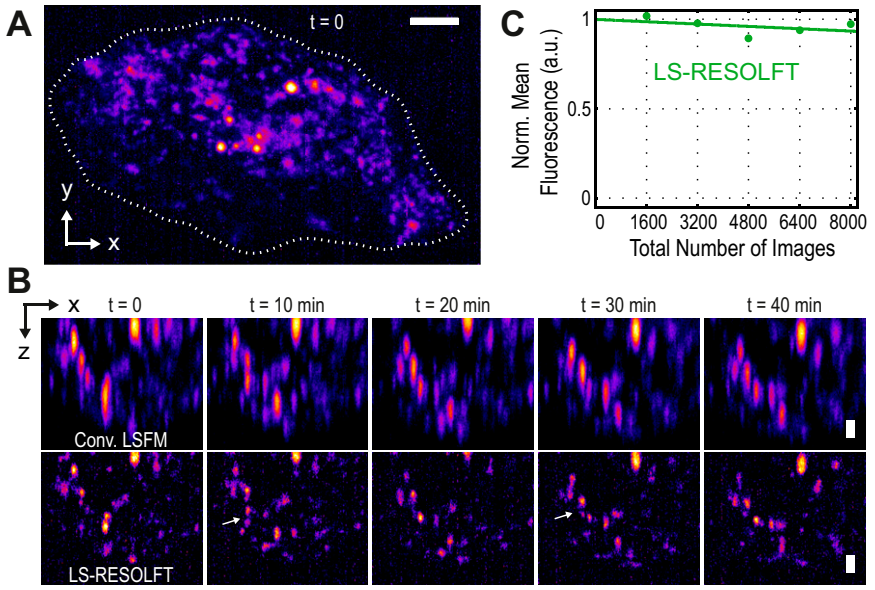

Fig. S8. Live-cell LS-RESOLFT imaging of HIV-1 assembly sites. (*A*) The HIV-1 assembly at the cell membrane of a HeLa cell was recorded over more than 40 min in LS-RESOLFT and conventional LSFM mode. An *x-y* maximum intensity projection of an LS-RESOLFT image stack taken at a time point $t = 0$ serves as an overview image. A white dashed line marks the boundaries of the living cell. A total volume of $45 \times 26 \times 7.5\ \mu m^3$ was recorded and the voxel size is set to $108.3 \times 108.3 \times 50\ nm^3$. Square pixels are shown. (Scale bar, 5 μm.) (*B*) The maximum intensity projections along the illumination axis of five image stacks taken in conventional LSFM (*Top Row*) and LS-RESOLFT mode (*Bottom Row*) are shown. The images were cropped to a size of $19 \times 7.5\ \mu m^2$. (Scale bar width and height, 1 μm.) The same cell was recorded at a time interval of 10 min. The superior axial resolution of LS-RESOLFT reveals HIV-1 assembly sites which cannot be distinguished in diffraction-limited LSFM. Two of these regions in the cell are highlighted by white arrows. In a living cell, HIV-1 assembly sites imaged with LS-RESOLFT become accessible to observation in three dimensions over time. (*C*) LS illumination and the low switching fatigue of rsEGFP2 proteins contribute to the ability to record a total number of 8,000 frames of the same cell without significant reduction in mean fluorescence. The data points are fitted with a linear function.

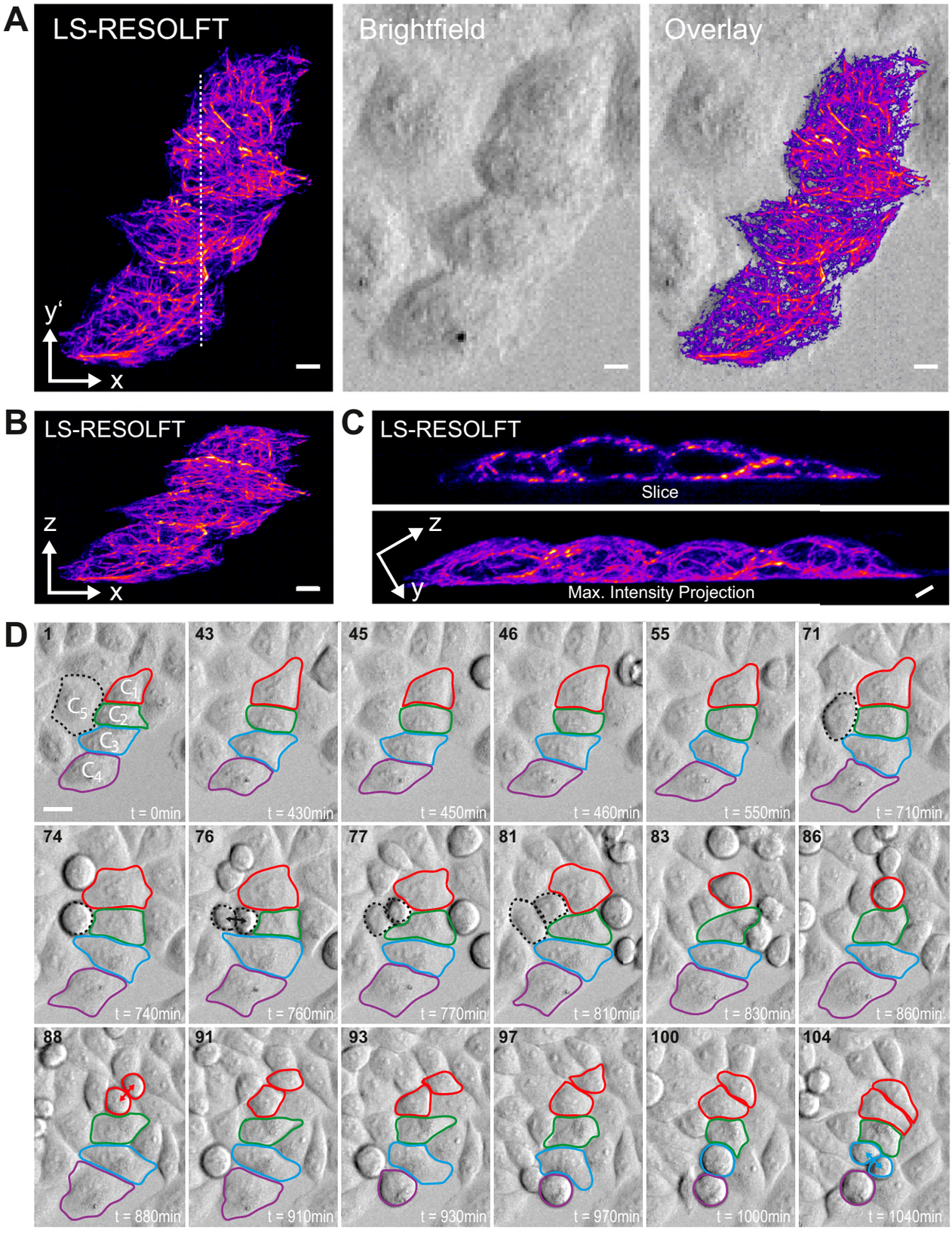

Fig. S9. Cell viability is not affected by LS-RESOLFT nanoscopy, as shown by occurrences of cell division. HeLa cells expressing keratin-19 fused to rsEGFP(N205S) imaged with LS-RESOLFT (using the same imaging parameters as in Fig. 3) exhibited no visual signs of photodamage (such as morphological changes, membrane blebbing, or other) upon imaging. Cell cycles were not arrested; cells throughout the imaged FOV (which is illuminated planewise with sequences of the activation, off-switching, and readout light) kept dividing, including the subset of transfected cells targeted for LS-RESOLFT nanoscopy. Unperturbed cell divisions are widely considered as the best indication for a low-stress cellular environment (and a "gold-standard" assay for cell viability). Directly after LS-RESOLFT nanoscopy (*A*–*C*), cells were transferred to an examination microscope (bright-field, Zeiss Cell Observer) and monitored at physiological conditions (37 °C, 5% CO_2) for many hours to assay the state of cells and register subsequent cell division events. (*D*) During a set observation period of 1,040 min (>17 h), several cells underwent division, as indicated by the color scheme with arrows for some divisions. Selected frames from a time-lapse experiment are shown; divisions occur both for transfected cells (C1–C4) and untransfected cells (an example is labeled as C5). (Scale bars in *A*–*C*, 5 μm.) A *y*-*z* slice through the cells along the white dashed line in *A* as well as a maximum intensity projection along the *x* axis is shown in *C*. (Scale bar in *D*, 20 μm.) The example shown is representative of our observations in four separate experiments.

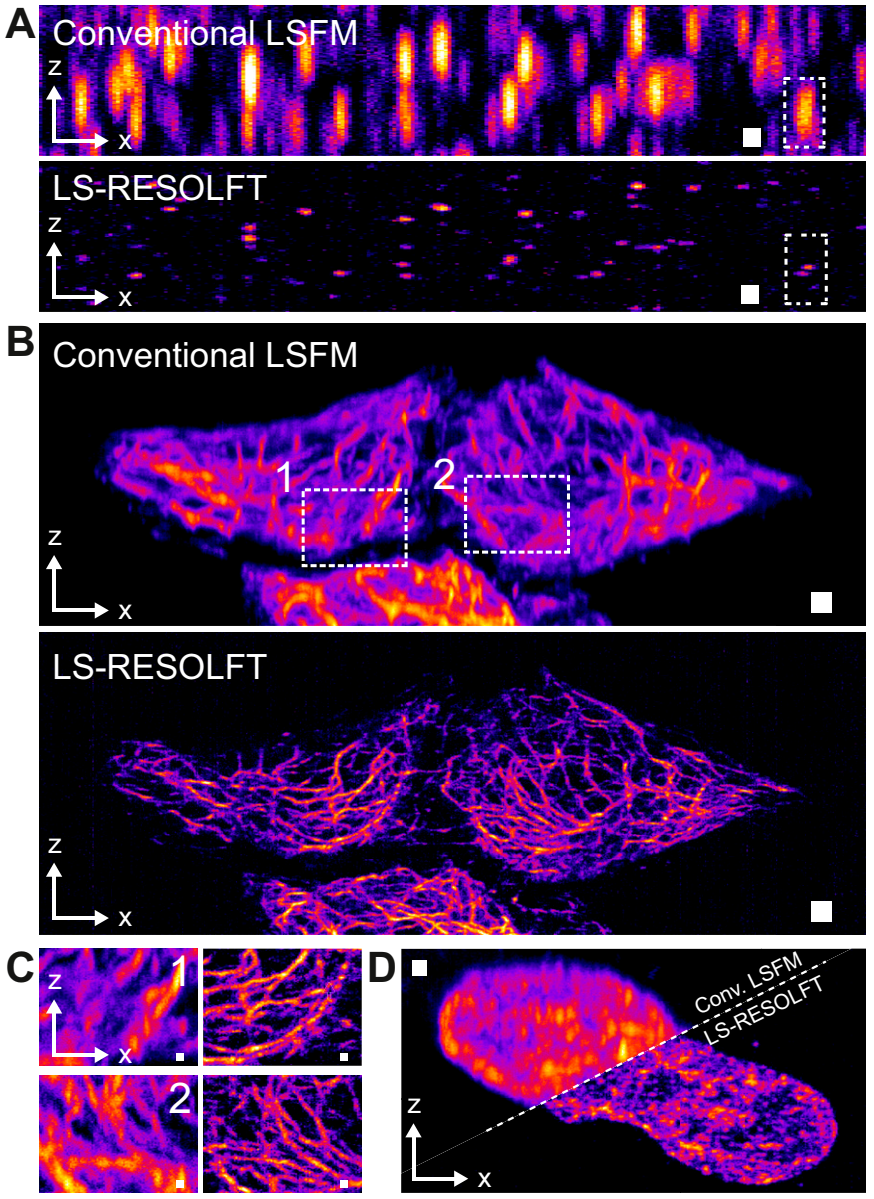

Fig. S10. LS-RESOLFT nanoscopy images from Figs. 2 and 3 rerepresented with isotropic pixels. (*A*) Replot of Fig. 2*A*. (*B*) Replot of Fig. 3*A*. (*C*) Replot of Fig. 3*B*. (*D*) Replot of Fig. 3*D*. (Scale bars are as indicated in the main figures.)

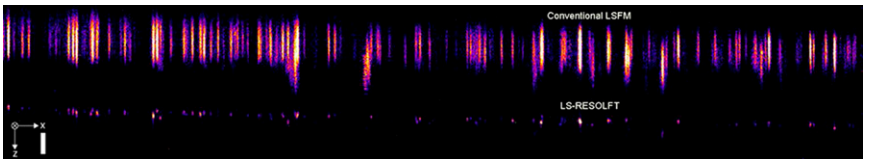

Movie S1. LS-RESOLFT nanoscopy data from Fig. 2*A*, rendered sectionwise ("fly-through" along *y* direction, total distance along *x*, 175 μm). Images were aligned to appear at the same *z*′ position. (Scale bar along *x* and *z*, 1 μm.)

Movie S1

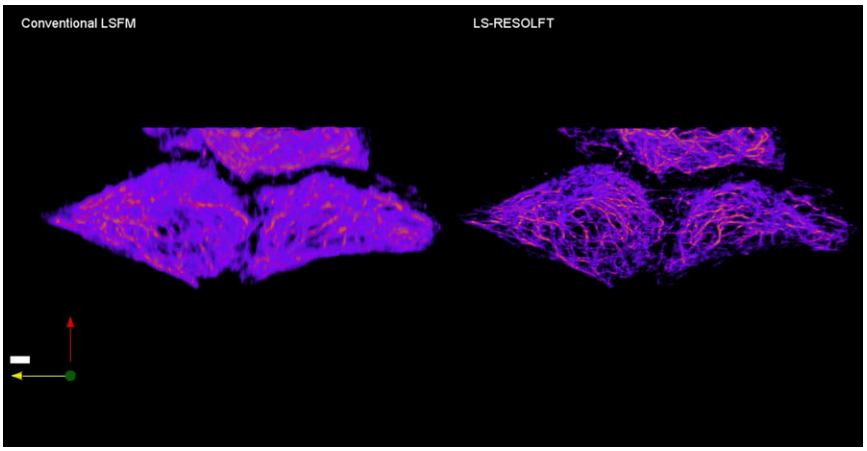

Movie S2. LS-RESOLFT nanoscopy data from Fig. 3*A* represented with isotropic pixels, shown rotating. (Scale bar along *x*, 3 μm; yellow, *x*; green, *y*; red, *z*.)

Movie S2

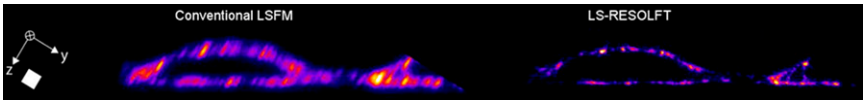

Movie S3. LS-RESOLFT nanoscopy data from Fig. 3*A* represented with isotropic pixels, rendered sectionwise (fly-through along *x* direction). (Scale bar along *y* and *z*, 2 μm.)

Movie S3